Translation position determination in ptychographic coherent diffraction imaging

Fucai Zhang,[1,2,3,*] Isaac Peterson,[1,4] Joan Vila-Comamala,[5,6] Ana Diaz,[5] Felisa Berenguer,[1,7] Richard Bean,[1,8] Bo Chen,[1,3] Andreas Menzel,[5] Ian K. Robinson,[1,3] and John M. Rodenburg[2,3]

[1] *London Centre for Nanotechnology, UCL, London, WC1H 0AH, UK*
[2] *Department of Electronic & Electrical Engineering, University of Sheffield S1 3JD, UK*
[3] *Research Complex at Harwell, Harwell Oxford, OX11 0FA, UK*
[4] *School of Physics, University of Melbourne, Victoria 3010, Australia*
[5] *Paul Scherrer Institut, 5232 Villigen PSI, Switzerland*
[6] *Current address: Diamond Light Source Ltd, Harwell, OX11 0DE, UK*
[7] *Current address: Synchrotron Soleil, L'Orme des Merisiers, Saint-Aubin, 94192 Gif-sur-Yvette*
[8] *Current address: Center for Free-Electron Laser Science, Notkestr. 85, 22607 Hamburg*
[*] *fucai.zhang@ucl.ac.uk*

Abstract: Accurate knowledge of translation positions is essential in ptychography to achieve a good image quality and the diffraction limited resolution. We propose a method to retrieve and correct position errors during the image reconstruction iterations. Sub-pixel position accuracy after refinement is shown to be achievable within several tens of iterations. Simulation and experimental results for both optical and X-ray wavelengths are given. The method improves both the quality of the retrieved object image and relaxes the position accuracy requirement while acquiring the diffraction patterns.

OCIS codes: (100.5070) Phase retrieval; (170.3010) Image reconstruction techniques; (340.7440) X-ray imaging.

References and links

1. H. M. L. Faulkner and J. M. Rodenburg, "Movable aperture lensless transmission microscope: a novel phase retrieval algorithm," Phys. Rev. Lett. **93**, 023903/1 (2004).
2. J. M. Rodenburg and H. M. L. Faulkner, "A phase retrieval algorithm for shifting illumination," Appl. Phys. Lett. **85**, 4795-4797 (2004).
3. J. M. Rodenburg, "Ptychography and related diffractive imaging methods," Advances in Imaging and Electron Physics **150**, 87–184 (2008).
4. J. M. Rodenburg, A. C. Hurst, A. G. Cullis, B. R. Dobson, F. Pfeiffer, O. Bunk, C. David, K. Jefimovs, and I. Johnson, "Hard X-ray lensless imaging of extended objects," Phys. Rev. Lett. **98**, 034801 (2007).
5. P. Thibault, M. Dierolf, A. Menzel, O. Bunk, C. David, and F. Pfeiffer, "High-resolution scanning X-ray diffraction microscopy," Science **321**, 379–382 (2008).
6. K. Giewekemeyer, P. Thibault, S. Kalbfleisch, A. Beerlink, C. Kewish, M. Dierolf, F. Pfeiffer, and T. Salditt, "Quantitative biological imaging by ptychographic x-ray diffraction microscopy," Proc. Natl. Acad. Sci. U.S.A. **107**, 529–534 (2010).
7. M. Dierolf, A. Menzel, P. Thibault, P. Schneider, C.M. Kewish, R. Wepf, O. Bunk, and F. Pfeiffer, "Ptychographic x-ray computed tomography at the nanoscale," Nature **467**, 436–439 (2010).
8. C. M. Kewish, P. Thibault, M. Dierolf, O. Bunk, A. Menzel, J. Vila-Comamala, K. Jefimovs, and F. Pfeiffer, "Ptychographic characterization of the wavefield in the focus of reflective hard x-ray optics," Ultramicroscopy **110**, 325–329 (2010).
9. E. Lima, A. Diaz, M. Guizar-Sicairos, S. Gorelick, P. Pernot, T. Schleier, and A. Menzel, "Cryo-scanning x-ray diffraction microscopy of frozen-hydrated yeast," Journal of Microscopy **249**, 1-7 (2013).
10. C. T. Putkunz, A. J. D'Alfonso, A. J. Morgan, M. Weyland, C. Dwyer, L. Bourgeois, J. Etheridge, A. Roberts, R. E. Scholten, K. A. Nugent, and L. J. Allen, "Atom-scale ptychographic electron diffractive imaging of boron nitride cones," Phys. Rev. Lett. **108**, 073901 (2012).

11. F. Hue, J. M. Rodenburg, A. Maiden, F. Sweeney, and P. A. Midgley, "Wave-front phase retrieval in transmission electron microscopy via ptychography," Phys. Rev. B **82,** 121415(R) (2010).
12. M. J. Humphry, B. Kraus, A. C. Hurst, A. M. Maiden, and J. M. Rodenburg, "Ptychographic electron microscopy using high-angle dark-field scattering for sub-nanometre resolution imaging," Nat. Commun. **3**, 9-13 (2012).
13. P. Thibault, M. Dierolf, O. Bunk, A. Menzel, and F. Pfeiffer, "Probe retrieval in ptychographic coherent diffractive imaging," Ultramicroscopy **109**, 338-343 (2009).
14. A. M. Maiden, J. M. Rodenburg, "An improved ptychographical phase retrieval algorithm for diffractive imaging," Ultramicroscopy, **109**, 1256-1262 (2009).
15. M. Guizar-Sicairos and J. R. Fienup, "Phase retrieval with transverse translation diversity: a nonlinear optimization approach," Opt. Express **16**, 7264–7278 (2008).
16. P. Thibault and M. Guizar-Sicairos, "Maximum-likelihood refinement for coherent diffractive imaging," New J. Phys. **12**, 063004 (2012).
17. F. Hue, J. M. Rodenburg, A. M. Maiden, and P. A. Midgley, "Extended ptychography in the transmission electron microscope: possibilities and limitations," Ultramicroscopy **111**, 1117-1123 (2011).
18. A. C. Hurst, T. B. Edo, T. Walther, F. Sweeney, and J. M. Rodenburg, "Probe position recovery for ptychographical imaging," J. Phys.: Conf. Ser. **241**, 012004 (2010).
19. A. Shenfield and J. M. Rodenburg, "Evolutionary determination of experimental parameters for ptychographical imaging," J. Appl. Phys. **109**, 124510 (2011).
20. A. M. Maiden, M. J. Humphry, M. C. Sarahan, B. Kraus, and J. M. Rodenburg, "An annealing algorithm to correct positioning errors in ptychography," Ultramicroscopy **120**, 64-72 (2012).
21. M. Beckers, T. Senkbeil, T. Gorniak, K. Giewekemeyer, T. Salditt, and A. Rosenhahn, "Drift correction in ptychographic diffractive imaging," Ultramicroscopy **126,** 44-47 (2013).
22. M. Guizar-Sicairos, S. T. Thurman, and J. R. Fienup, "Efficient subpixel image registration algorithms," Opt. Lett. **33,** 156–158 (2008).
23. M. Dierolf, P. Thibault, A. Menzel, C. M. Kewish, K. Jefmovs, I. Schlichting, K. V. Koenig, O. Bunk, and F. Pfeiffer, "Ptychographic coherent diffractive imaging of weakly scattering specimens," New J. Phys. **12**, 035017 (2010).
24. F. Zhang and J. M. Rodenburg, "Phase retrieval based on wave-front relay and modulation," Phys. Rev. B **82**, 121104(R) (2010).
25. S. Gorelick, J. Vila-Comamala, V. A. Guzenko, R. Barrett, M. Salomé, and C. David, "High-efficiency Fresnel zone plates for hard X-rays by 100 keV e-beam lithography and electroplating," J. Synchrotron Rad. **18**, 442-446 (2011).
26. F. Zhang, G. Pedrini, and W. Osten, "Phase retrieval of arbitrary complex-valued fields through aperture-plane modulation," Phys. Rev. A **75**, 043805 (2007).
27. X. Huang, M. Wojcik, N. Burdet, I. Peterson, G. Morrison, D. Vine, D. Legnini, R. Harder, Y. Chu, and I. Robinson, "Quantitative X-ray wavefront measurements of Fresnel zone plate and K-B mirrors using phase retrieval," Opt. Express **20**, 24038-24048 (2012).
28. P. Thibault and A. Menzel, "Reconstructing State Mixtures From Diffraction Measurements," Nature **494**, 68–71 (2013).

1. Introduction

Ptychography is a recent development of the lensless coherent diffraction imaging (CDI) technique that alleviates the convergence difficulty of conventional methods by recording multiple diffraction patterns of an object with overlapping illuminated regions [1-3]. Ptychography has been successfully demonstrated with photons at visible and X-rays wavelengths [4-9], and more recently with electrons [10-12]. Various kinds of samples, ranging from nano-particles to biological cells, have been imaged using this method.

The *a priori* information required in ptychography is the illumination probe function and the lateral translations of the object relative to the probe. Recent progress in reconstruction algorithms was aimed to alleviate the rigorous requirement of knowing them. A rough initial guess of the probe function usually suffices for a successful reconstruction [5, 13-15]. The translation errors are difficult to tackle experimentally, especially when imaging with X-rays and electrons. For instance, in electron ptychography the beam must be controlled with 50 pm accuracy, which is almost impossible to achieve in the presence of thermal drift (usually non-linear and of the order of nanometers per minute) and/or hysteresis in the probe scan coils. Translation position optimization along with object and probe reconstruction was first

introduced in [15]. However, the slow convergence of this optimization approach suggests its use being as final refinement after other algorithms have approximately determined the object and the probe function [16].The influence of position errors in ptychography has also been analyzed by Hue et al. in the context of electron experiments [17]. They found that an error of only a fraction of the required resolution could seriously degrade the reconstruction quality. Some other preliminary attempts to correct such errors have only limited success, and often rely on human intervention [18] or are computationally intensive [19]. The recently proposed "annealing" approach based on a trial-and-select strategy provides a promising solution to this problem [20]. A method has also been shown effective if a model of position error can be provided [21].

In this paper we present a different, yet simple and efficient position determination method for ptychography. It works with poorly defined initial probes as well. Sub-pixel refinement accuracy is achievable for initial errors as large as about the nominal translation step or photon counts as low as a few tens of thousands per diffraction pattern. The paper is organized as follows: section 2 details the position determination method implemented as an addition to the extended ptychographical iterative engine algorithm [14]; section 3 evaluates the performance of the algorithm in simulation; experimental results are given in section 4; discussion and conclusion are given at the end.

2. The position determination algorithm

In ptychography, a sequence of diffraction patterns is recorded as the specimen steps transversely across a localized probe. The translation steps are kept smaller than the probe size so that the adjacent illuminated regions have some overlap. We denote the illumination probe and the specimen transmission functions as P(r) and O(r), respectively. Assuming the thin-object approximation, the exit wavefield just behind the specimen is then given by

$$\psi^j(\mathbf{r}) = P(\mathbf{r})O(\mathbf{r},\mathbf{s}_j) \tag{1}$$

where $\mathbf{r}=(x,y)$ is the coordinate vector at the object plane and $\mathbf{s}_j$ is the j^{th} object translation shift. The exit wave propagates to the detector. The measured intensity is

$$I_j(\mathbf{u}) = \left|F\left\langle\psi^j(\mathbf{r})\right\rangle\right|^2, \quad j=1,\ 2,\ ...,\ J \tag{2}$$

where, **u** denotes the coordinate vector at the detector plane, and J is the total number of diffraction patterns. The symbol $F<>$ represents the beam propagation operator. For far-field diffraction, it is the Fourier transform.

The task of ptychographic reconstruction algorithms is to search for suitable object and probe functions that can fulfil two sets of constraints associated with the recorded data: the modulus constraint in the detector plane and a consistency requirement in the overlapping regions of object reconstructions that is referred to as overlap constraint in this paper.

Several iterative phase retrieval schemes have been proposed for reconstructing ptychographical datasets. These include the original and extended ptychographical iterative engines (PIE and ePIE) [2, 14], the difference map method [5, 13], and the global optimization methods [15]. Here we utilize the ePIE algorithm as an example to explain the principle of our position determination method.

In the ePIE algorithm, the updating operation of object and probe functions are performed serially for each diffraction pattern. The iteration starts with initial guesses of $O_0(\mathbf{r})$, $P_0(\mathbf{r})$ and proceeds as follows for the m^{th} iteration,

1) Form an exit wave $\psi_m^j(\mathbf{r})$ according to Eq. 1 for the j^{th} object position.

2) Propagate the exit wave to the detector, yielding a diffracted field denoted as $\Psi_m^j(\mathbf{u})$.

3) Replace the modulus of the diffracted field with the square-root of the j^{th} measured intensity,

$$\tilde{\Psi}_m^j(\mathbf{u}) = \Psi_m^j(\mathbf{u}) \Big/ |\Psi_m^j(\mathbf{u})| \cdot \sqrt{I_j(\mathbf{u})}. \tag{3}$$

4) Form a revised exit-wave estimate by back-propagating the revised diffracted wave to the object plane

$$\tilde{\psi}_m^j(\mathbf{r}) = F^{-1}\left\langle \tilde{\Psi}_m^j(\mathbf{u}) \right\rangle. \tag{4}$$

Steps 2-4 implement the modulus constraint.

5) Apply the overlap constraint to form a revised object estimate

$$O_{m+1}(\mathbf{r}, \mathbf{s}_j) = O_m(\mathbf{r}, \mathbf{s}_j) + \alpha_1 \frac{P_m^*(\mathbf{r})}{|P_m(\mathbf{r})|^2_{\max}} \left[\tilde{\psi}_m^j(\mathbf{r}) - \psi_m^j(\mathbf{r}) \right] \tag{5}$$

where the parameter α_1 takes value within [0, 1.5], a range empirically found giving good algorithmic convergence. Compared to the Wiener-type weighting function in the original PIE algorithm [2], this new form $P_m^*(\mathbf{r}) \Big/ |P_m(\mathbf{r})|^2_{\max}$ has been shown to be robust and usually leads to rapid convergence in various situations [14].

6) Update the entire object function $O(\mathbf{r})$.

7) Apply the overlap constraint to form a revised probe estimate when a rough estimate of object has been obtained.

$$P_{m+1}(\mathbf{r}) = P_m(\mathbf{r}) + \alpha_2 \frac{O_m^*(\mathbf{r}, \mathbf{s}_j)}{|O_m(\mathbf{r}, \mathbf{s}_j)|^2_{\max}} \left[\tilde{\psi}_m^j(\mathbf{r}) - \psi_m^j(\mathbf{r}) \right] \tag{6}$$

where the parameter α_2 takes a value usually smaller than α_1, accounting for the fact that the probe will be updated more frequently than the object.

The process above repeats for the next object position $\mathbf{s}_{j+1}$ until all scan positions have been reached to complete a single iteration step.

In the presence of translation position errors, we observed that the revised individual object estimate $O_{m+1}(\mathbf{r}, \mathbf{s}_j)$ in fact shifts towards its true position after the enforcement of the modulus and the overlap constraints. The reconstruction artefacts due to the position errors occur mainly in the step of stitching each individual reconstruction to form the entire object. The relative shift $\mathbf{e}_{j,m}$ between $O_{m+1}(\mathbf{r}, \mathbf{s}_j)$ and $O_m(\mathbf{r}, \mathbf{s}_j)$ is very small but provides a useful signal that can be fed back to correct $\mathbf{s}_j$. A new step is then added after step 5,

$$\mathbf{s}_{j,m+1} = \mathbf{s}_{j,m} + \beta \cdot \mathbf{e}_{j,m} \tag{7}$$

where the parameter β could be either a constant or a function of the iteration number that amplifies the position error signal to control the rate of refinement.

The shift error $\mathbf{e}_{j,m}$ is obtained by locating the peak of the cross correlation function

$$C(\mathbf{t}) = \sum_{\mathbf{r}} O_{m+1}(\mathbf{r}, \mathbf{s}_{j;m}) \Pi_m(\mathbf{r}) O_m^*(\mathbf{r} - t, \mathbf{s}_{j;m}) \Pi_m^*(\mathbf{r} - \mathbf{t}) \tag{8}$$

where the binary function $\Pi(\mathbf{r})$ specifies the object area through which the light has considerable contribution to the diffraction pattern. It can be calculated by setting a threshold (e.g. 0.1 of the maximum magnitude) on the probe modulus.

To reduce the computation time, Eq. 8 is evaluated in the Fourier domain according to the convolution theorem; that is calculating the product of the spectra of the current and revised object estimates and then taking its inverse Fourier transform. The magnitude of the shift error signal $\mathbf{e}_{j,m}$ is typically in the order of 0.01 pixels or less in our various simulations and reconstructions with real data. Such high precision is achieved using the matrix multiplication method proposed by Guizar-Sicairos et al. [22], which reduces the computation complexity dramatically.

Cross-correlation techniques are widely used in image registration. Here, however, it is worth noting that in our algorithm the cross-correlation is not performed by aligning the overlapped regions of object reconstructions at two adjacent scan positions. Instead, it is on two successive iterations of the object at the same scan position. The convergence of the algorithm might be understood from Cauchy's limit theorem, which states that the elements in a converging sequence become arbitrarily close to each other as the sequence progresses. Here for each diffraction pattern, i.e., scan position, a sequence of position estimates is formed. The sequence will have decreasing distance between adjoining elements when approaching to its limit. The fact that the overlapped region of object from different measurements needs to be aligned is implicitly performed by the overlap constraint along with the modulus constraint in the algorithm. To emphasize this point, we call the method "serial cross-correlation".

3. Simulation and performance analysis

3.1 Simulation

The performance of the algorithm was first evaluated with simulated diffraction data. The parameters we chose simulate a typical visible-light experiment. The probe was formed from an 800 μm pinhole illuminated with light of wavelength 400 nm and placed 9 mm upstream of the object. The two images in Figs. 1(a) and 1(b), consisting of 492×492 pixels, were respectively used for the modulus and the phase of the object. Its modulus ranges from 0.3 to 1 and its phase from $-\pi$ to π. The detector had 256×256 pixels of a size 10 μm across and was located 50 mm downstream from the object.

Different translation error patterns were tested, including a rotation of the overall positions, a shear of the overall positions in one direction as would be caused by drift and uncorrelated random errors at each position. As an illustration, the position map in Fig. 2 was used for the results given in the paper. The green circles indicate the positions used to generate the diffraction patterns, which were generated from a 9×9 regular grid with random offset added to avoid the raster grid pathology artifact [23]. The grid interval and the maximum of random offset were 23 pixels and 8 pixels, respectively.

In conjunction with updating the object function, we ran the simulation for three cases: updating the probe function only; updating the translation position only; and updating both. In all cases, the initial probe function guess was a round disk with constant phase and amplitude. The diameter of the round disk indicated by a yellow dashed circle in the inset of Fig. 1(a) was chosen to be larger than the extent of probe having significant values. The initial position guesses, indicated by red dots in Fig. 2, were generated from the actual ones (green circles) by adding values to their coordinate randomly taken from [-23, 23] in both the x and y directions. The feedback parameter β was adjusted automatically as described in the following Section 3.2. The initial object estimate had constant amplitude and phase. We began the translation position and the probe function updates on the 3rd and 60th iteration, respectively. The total number of iterations was 300 in all cases.

Figures 1(c)-1(h) show the reconstructed images for all the three cases. The reconstructed probe functions are also shown as insets with center pixel set to 0, in range of $[-\pi\ \pi]$. When only updating the probe function, the reconstructed object and probe functions are seriously distorted, as shown in Figs. 1(c) and 1(d). When updating the positions but holding the initial probe estimate constant, the positions were actually recovered to good accuracy after 85

iterations (see movie Media 1). The blurring in Figs. 1(e) and 1(f) is mainly due to the incorrect estimate of probe function. When both position and probe update were carried out, much better reconstructions of both object and probe were obtained and shown as Figs. 1(g) and 1(h).

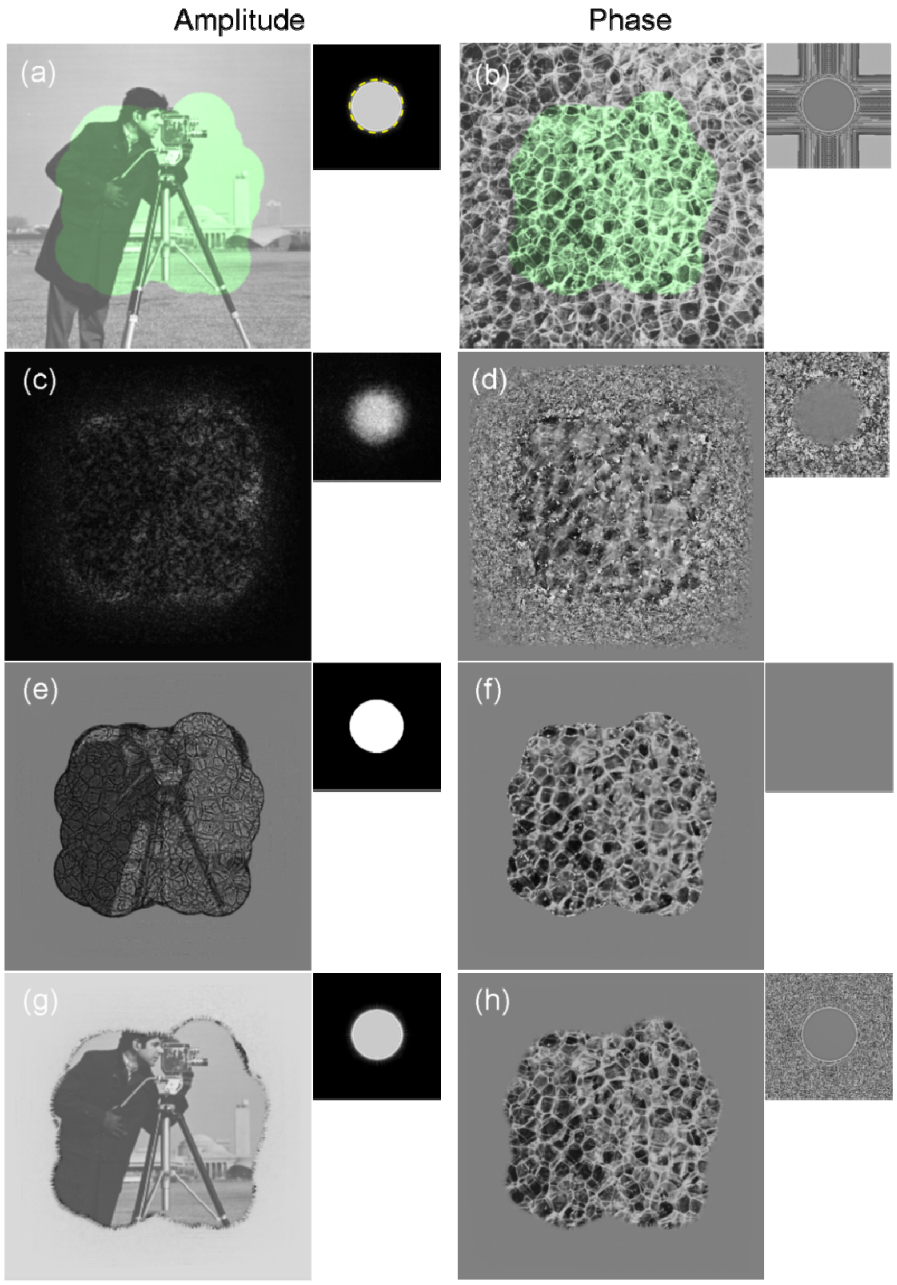

Fig. 1. Comparison of reconstruction quality with or without position refinement. (a) and (b) Test object modulus [0.3, 1] and phase [-π, π]. Insets are the probe amplitude and phase respectively. The highlighted areas indicate the measured region of object. (c) and (d) Reconstructed images with probe function update only. (e) and (f) Reconstructed images with position update only. (g) and (h) Reconstructed images with both probe function and translation position update. A movie, Media 1, showing the reconstruction process is available online.

The blue lines in Fig. 2 and also in the movie, Media 2, illustrate the position recovery vector during the iterative process with the final positions indicated by red pluses. We note that, for most of the scan positions, the positions were recovered by almost the shortest route, i.e., in a straight line. The mean error of retrieved positions was calculated as 0.0035 pixels. The computation time, on a desktop PC with an Intel Xeon CPU, for probe function updating only and updating both were 305 s and 430 s, respectively. As shown in the movie, most of the positions were hardly refined after 85 iterations. When the position update was disabled after iteration 85, the total reconstruction time reduced to 368 s.

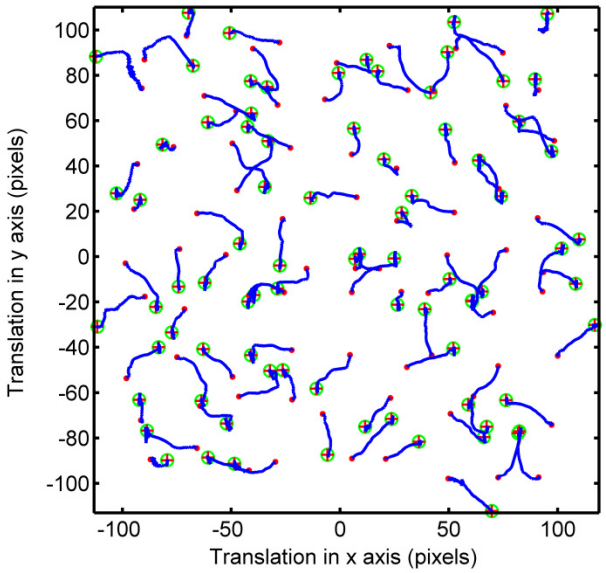

Fig. 2. Position maps used in the simulation. The green circles indicate the actual positions used in generating the diffraction data. The red dots and red pluses indicate the positions before and after position refinement, respectively. The blue lines illustrate the traces retrieved at each iteration step. The mean initial translation error is 17.7 pixels. A movie is available online, Media 2.

3.2 Effect of feedback parameter

The feedback parameter β is an important parameter whose value needs to be set properly in the algorithm. The effect of β on the convergence rate of position refinement is shown in Fig. 3. The position errors were calculated as the mean value of the distance between the retrieved and the actual ones over all scan positions. The possible global shift in the retrieved positions was removed by aligning its central one with its counterpart of the actual ones. For each setting of β, two plots are given: without and with probe function update indicated by the red dashed and the blue solid lines, respectively.

The parameter β usually is significantly larger than unity because the retrieved shift between iterations, $\mathbf{e}_{j,m}$, is much smaller than the actual error in position, especially in the early stage of the reconstruction when the object and the probe functions have not been well retrieved. Without probe function update (red dashed lines in Fig. 3(a), the rate of position refinement improves monotonically as β increases as long as β has moderately small value, e.g. β=50 or β=200. The trend continues until a certain value is reached, here at $\beta\approx$300, above which the position error starts to oscillate and stagnates at relatively high value, about 0.4 pixels because over-feedback leads to instability. The red dashed line for β=400 illustrates this phenomenon. The optimal value β depends on the actual probe and object functions and may take a value from one to several hundreds. For structure-rich probe and object, a small β

suffices for a rapid refinement; whilst for smooth sample and probe, a larger value is required to achieve a similar rate of refinement.

When investigating the interplay between the probe update and the position update, we observed that the position update is much less sensitive to incorrect initial probe function estimates than the probe function update to incorrect initial position estimates. Therefore, the position update should start before the probe function update. At what iteration number the probe function update should be started depends on the setting of β. The smallest value of β, at which oscillation would occur, reduces when probe update is allowed (see the plot β=200). Plots in Fig. 3(a) illustrate all those observations. When β=50, the mean error reduces rapidly and monotonously to a much lower value with probe updating. For β=200, the error first decreases and then oscillates at relatively high level of errors about 0.5 (blue solid line). This phenomenon is even more apparent for the case of β=400. This means, by the time the probe function update is to be started, the positions should be approximately accurate.

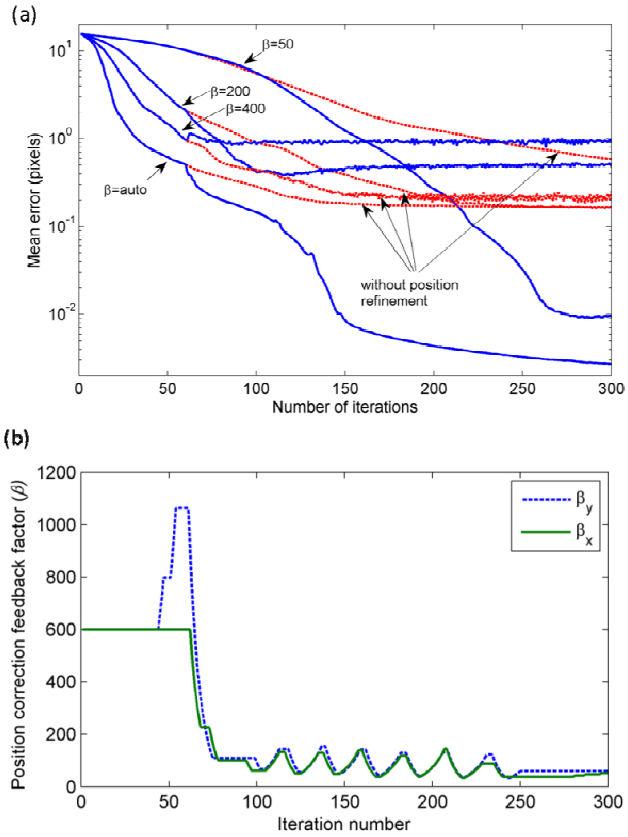

Fig. 3. (a) Evolution of position error for various β settings with (blue solid lines) and without (red dashed lines) probe update. The probe update started at the iteration 60. (b) Evolution of feedback parameter β value with the iteration number in the case of automatic adjustment of β.

To achieve an overall fast refinement rate and small residual error, one could employ a large β at the beginning and then gradually decrease it to avoid the occurrence of oscillation. A simple automatic method for β adjustment was implemented. The cross-correlation coefficient between two sets of successive retrieved position errors was calculated (for x and y direction separately), referred as κ here. A positive κ implies that the two refinements go in the 'same' direction and the value of β could be increased to accelerate the refinement rate. In contrast, a negative κ indicates that the feedback mechanism oscillates and becomes unstable

and the value of β should be reduced. In our implementation, when κ was greater than 0.3, β was increased by 1.1 times to accelerate the refinement. When κ was less than -0.3, it was decreased by a factor of 0.9. The actual value of the preset thresholds (here, ±0.3) is not critical. The improvement of using automatically adjusted β is shown in Fig. 3(a). In the case without probe function update, it reached the same error as with β=200 but at a much faster rate. The remaining error is mainly due to the incorrect probe. When the probe function update was allowed, a much lower position error, i.e., 0.0035 pixels was achieved. Plots in Fig. 3(b) show the evolution of β as the iteration progresses.

3.3. The maximum allowable initial position errors

The mean position errors after refinement for varied magnitude of starting position errors are shown in Fig. 4. Poisson noise was included in the simulation with total counts in the probe set to 10^8. All other simulation parameters were the same as above and we used automatic adjustment for the β parameter. For mean start error less than 19.5 pixels, the algorithm retrieves the correct positions to within 0.004 pixels of their true value. We also note that the residual errors are nearly independent of the initial errors. The green line at the bottom of Fig. 4(b) shows the residual error at each scan position for the case of an initial magnitude of 19.3 pixels. For larger initial errors, comparable to the scan spacing itself, the mean retrieved error starts to increase abruptly. However, as shown by the circle and square headed stem plots in Fig. 4(b), errors larger than 1 pixel occurred only at the boundary area for which the overlap is known to be small. For example, in the case of an initial error of 21.6 pixels, only two positions, indexed at 55 and 63, had residual errors larger than 1 pixel. At all other positions, the errors are still very low. The higher errors than the case of an initial error of 19.3 pixels is attributed to the degraded probe estimate caused by updating from those scan positions with big position errors.

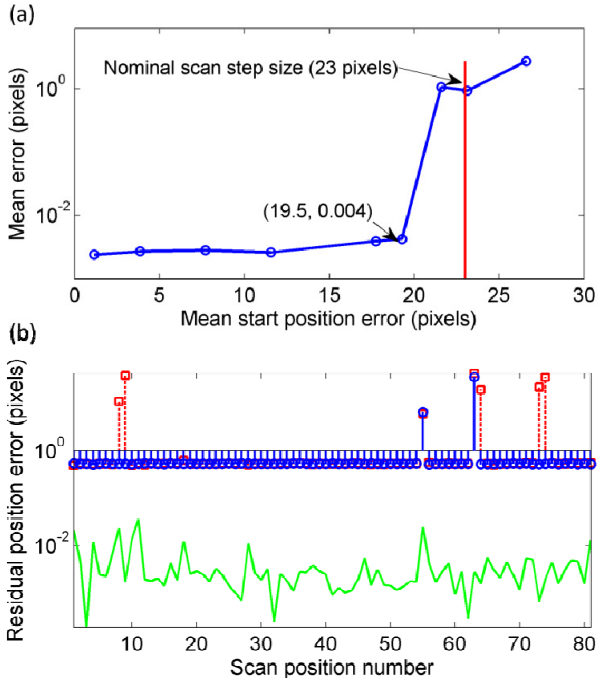

Fig. 4. Dependence of residual position error on the magnitude of initial position error. (a) Mean residual error versus the initial position error. (b) Residual error at each scan positions for the three magnitudes of initial position errors: 19.28 pixels (green line); 21.6 pixels (circle headed blue line); and 26.6 pixels (square headed red line).

3.4. Effect of Poisson noise

The effect of Poisson noise in the diffraction data on the accuracy of retrieved position was evaluated with the same parameters as above except that the mean error of initial position guesses was reduced to 9 pixels. The x and y coordinates error randomly taking values within [-13, 13] with equal probability. We ran the simulation eight times with varied number of photons in the probe. As shown in Fig. 5, the mean position error decreases logarithmically with a slope of 0.78 from 7.5 pixels to 0.0054 pixels whilst the count increased from 10^3 to 10^7. The reduction became mild for further increase of photon number and at the value of 10^9 it reduced to 0.0025 pixels, which is about 3500 times smaller than the start error. The required count for a residual error below 1 pixel is 1.03×10^4. Note that at such low photon count the reconstruction quality would degrade a lot and sub-pixel position errors as provided by our method would be hardly noticeable.

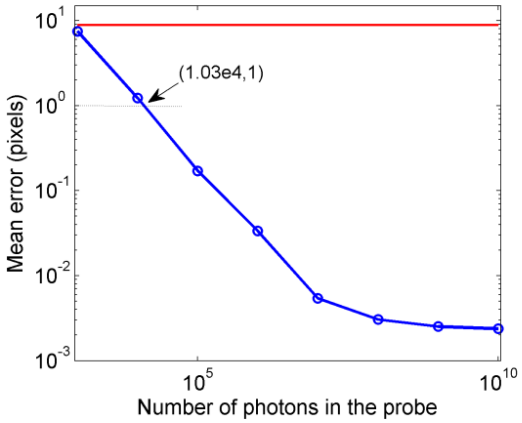

Fig. 5. Effect of Poisson noise on the accuracy of retrieved position. The red line (9 pixels) indicates the mean error of initial position guesses.

4. Experiment results

4.1 Visible-light experiment

The algorithm was tested with experimental data at optical and X-ray wavelengths. For the optical experiment, a ptychographic dataset was collected using a USAF 1951 resolution target sample. Due to the fine structure in the object, the reconstructions are highly sensitive to position errors and therefore suitable to demonstrate the accuracy of our algorithm. The target was mounted on an x/y translation stage assembly placed 10.6 mm downstream of an 800 μm pinhole. The wavelength of light was 635nm. A 14-bits charge-coupled device (CCD) detector with 7.4×7.4 μm^2 pixel size was placed 24 mm further downstream to collect the diffraction data. The sample was scanned over a 8×8 irregular grid formed from a 200 μm spaced grid with random offset in x- and y- directions, which had the maximum magnitude of 24 μm, corresponding to [-6, 6] pixels. To increase the dynamic range, additional frames, with 5 and 25 times increased exposure time, respectively, were recorded and combined for each scan position.

The central 512×512 pixel region from each diffraction pattern was used to reconstruct the target sample. The reconstruction was run for 200 iterations. Position and probe updates started at iteration 2 and 50 respectively. The regular grid positions with spacing 200 μm were used for the initial guess of scan positions. The parameter of β was adjusted automatically as described in section 3.2. The comparison of reconstructed images of the object in Fig. 6 clearly demonstrates the improvement due to the position refinement algorithm.

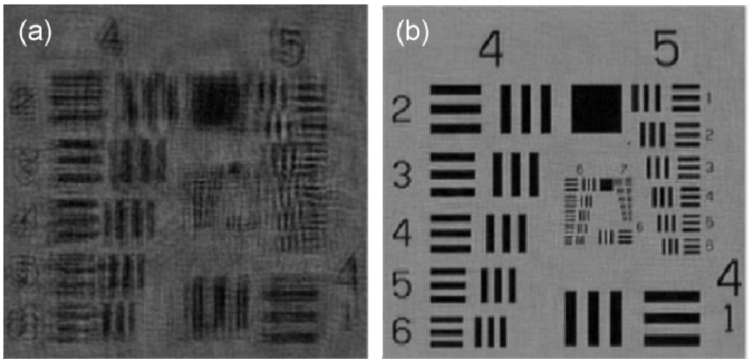

Fig. 6 Reconstructed images of a USAF 1951 target (a) without and (b) with position refinement.

4.2 X-ray experiment using Fresnel zone plate illumination

The algorithm was also tested with an X-ray diffraction dataset recorded with some accidental alignment errors. The experiment was performed at the cSAXS beamline at the Swiss Light Source (SLS), Paul Scherrer Institut, Villigen, Switzerland, with the aim to demonstrate a modulation coherent imaging (MCI) technique proposed by the authors [24]. In MCI, a known modulator is used to eliminate the convergence issues associated with the conventional phase retrieval methods using a single measurement, especially when applied to strong complex-valued samples. Here the modulator was a lithographically nano-fabricated phase plate consisting of gold blocks with a design pattern of random distribution on a grid of spacing 100 nm. The thickness of the Au structure was about 1.2 μm (measured with scanning electron microscopy, SEM) which gave a phase shift of π at beam energy of 6.2 keV, i.e., wavelength, λ=0.2 nm. A curved illumination was formed by an off-axis region, defined by a 20 μm entrance pinhole, of a Fresnel zone plate (FZP) with a focal length of 50 mm [25]. An order-sorting aperture of diameter 20 μm was placed about 2 mm in front of the beam focus. The modulator mounted on a 2D piezoelectric stage was placed 11.4 mm behind the focus. An optically coupled CCD detector with a columnar CsI scintillator, 1:1 taper was brought to the beamline. The detector had 1300×1340 pixels, each 20 μm in size, and was located 7.21 m downstream from the modulator for data acquisition.

Ptychographic datasets were recorded for the calibration of the modulator. A circular scan pattern with 5 points in the first shell and a radial increment of 1 μm between consecutive shells was used. The total 158 scan points covered an area of 14×14 μm^2. At each scan position, a diffraction pattern was recorded with an exposure time of 2 s, which makes a total of 5 minutes for a complete measurement. The measured diffraction data were binned by a factor 4 and zero-padded to 512×512, giving a pixel size of 35.2 nm in the reconstructed images.

The ePIE algorithm was run for 150 iterations with the probe update started at iteration 50. The transmission function of modulator calculated from its design parameters was used to start the reconstruction instead of a guessed probe [26]. Here the probe was left unknown and set to a random distribution. The reconstructed images, shown in Figs. 7(a) and 7(b), had poor and uneven quality over the field of view. The vertical strip enclosed by the dotted yellow lines indicates an area with slightly better quality than outside. More interestingly, we observed that the reconstructed probe actually moved when subsets of diffraction patterns corresponding to different object regions were used. Both uneven quality and probe motion indicated that the position values fed to the algorithm were not correct. When the above procedure was re-run with the position refinement enabled after iteration 2, a much improved reconstruction, shown in Figs. 7(c) and 7(d), was obtained. Because of the high aspect ratio of

the modulator, which was greater than 10, some fine structures of the modulator are either missing or collapsed, exhibiting a large amount of deviation from the original design. The thickness, derived from the reconstructed phase, is about 1.1 μm, which agrees with measurements by the scanning electron microscopy. Figs. 7(e) and 7(f) show the retrieved probes for comparison. The probe with position refinement had a smoother profile and more fringes up to higher angles.

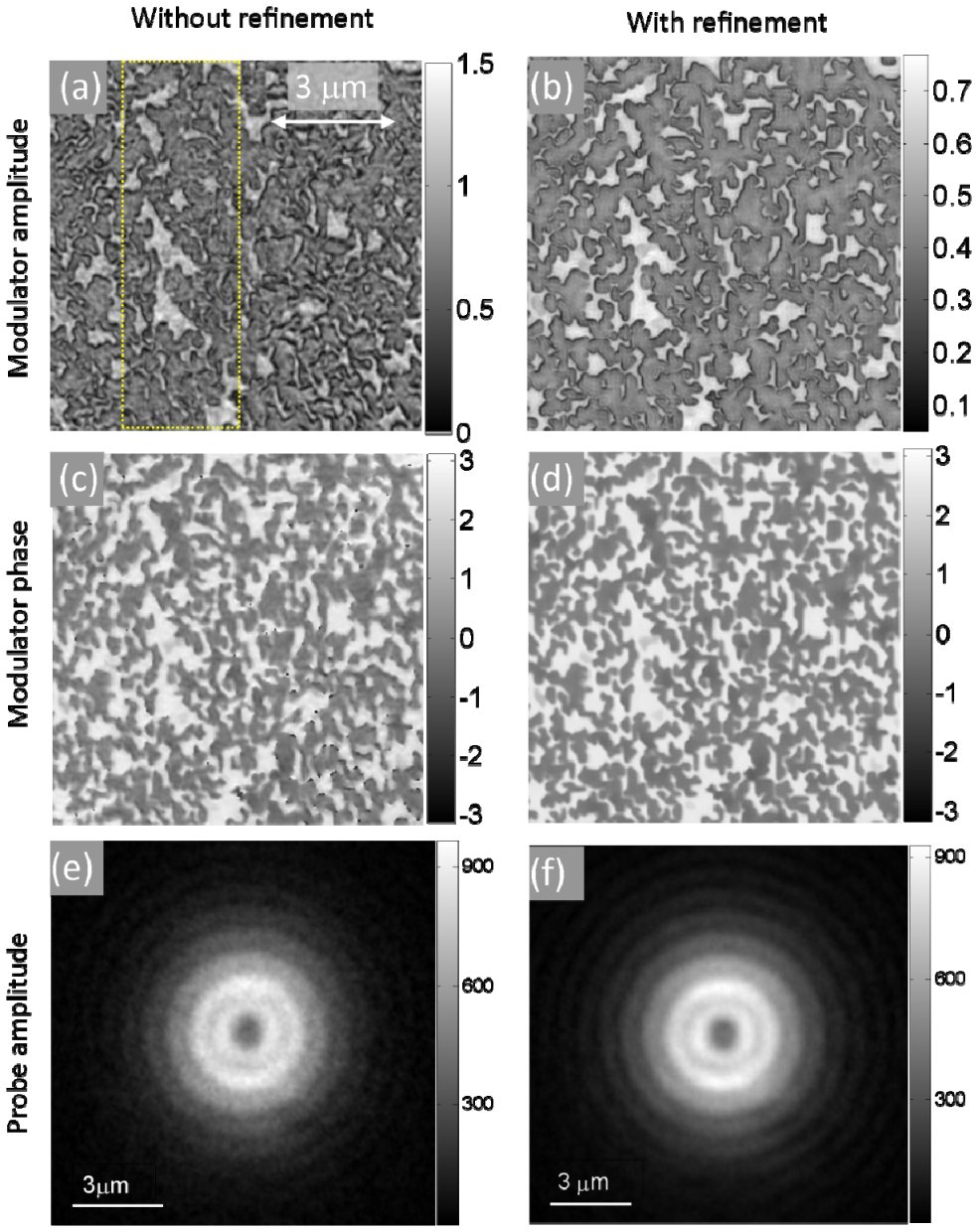

Fig. 7. Reconstructed images of a nano-fabricated random phase plate using X-ray data (cut-out of central region). (a) and (b) Reconstructed modulus of modulator without and with position refinement. (c) and (d) Reconstructed phase of modulator without and with positions refinement. (e) and (f) Reconstructed probe amplitude (cutout of central region) without and with position refinement.

Figure 8(a) shows the retrieved position errors along the *x* and *y* directions at each point in the scan. The periodic variation of error implies that it arises mainly from a systematic misalignment problem. Fig. 8(b) illustrates the initial and the retrieved *x*-*y* position maps. Noticeably, the corrected positions have a global rotation, anti-clockwise, with respect to the initial ones. The unequal error magnitude in the *x* and *y* axes in Fig. 8(a) or the shrinkage in lower left to upper right diagonal direction but expansion in upper left to lower right diagonal direction in Fig. 8(b) (shown by the arrows) indicates the presence of out-of-plane tilt errors. A simplistic analysis indicates misalignment of stage and detector by about 10˚ around both the vertical and the horizontal axes. The exact cause of these unusually big systematic deviations, however, is currently not understood.

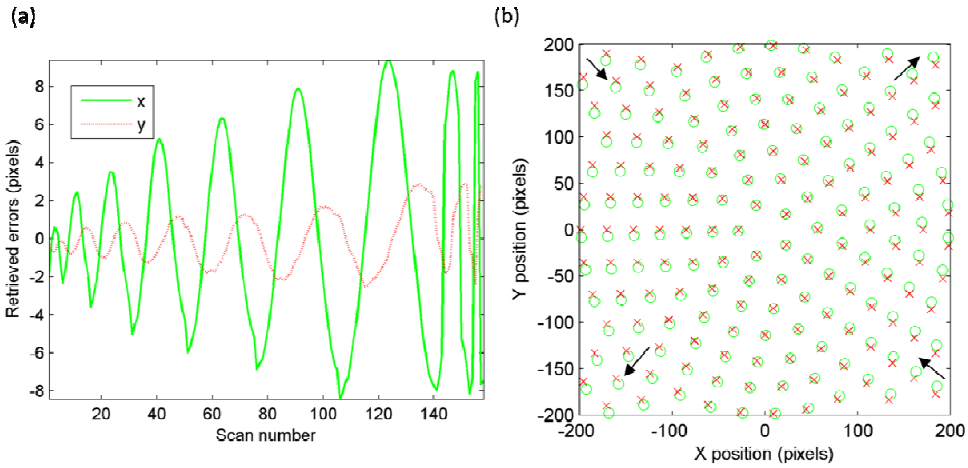

Fig. 8. (a) Retrieved translation position errors at each scan positions; (b) Position maps before (red crosses) and after (green circles) position refinement; a pixel is 35.2 nm wide.

4.3 X-ray experiment using Kirkpatrick-Baez (KB) mirror illumination

We performed a second test of the algorithm with X-ray data obtained at the Advanced Photon Source beamline 34-IDC. We used a similar experimental setup to that above, but used KB mirrors as the focusing optics, which generate a different shaped probe [27]. The sample was scanned through a 9 keV beam using an piezo stage, mounted above a set of XYZ step-motors, as well as a set of goniometer motors governing rotations about the *x*, *y*, and *z* axes. An entrance slit of 10×40 μm^2 was used in front of the KB mirrors to define the coherence. The scanning trajectory covered a 10×10 μm^2 area consisting of concentric circles with a radial increment of 0.5 μm and 5n equally spaced points in its nth ring, giving 323 scanning points in total. A "Siemens Star" design was lithographed into a 1.5 μm thick tungsten sheet on a Si_3N_4 membrane and used as a test sample. The resulting diffraction dataset was collected by a Princeton Instruments PI-MTE 1300B CCD with 20 μm square pixels, placed 2.0 m downstream of the sample. The acquisition time for each image was 0.1 s, and we summed up 5 images per scan position. The region of interest (ROI) in the diffraction patterns was set to be 256 × 256 pixels. This gives the pixel size in the sample plane of 54 nm.

We ran the ePIE algorithm for 200 iterations with initial probe guess obtained from a knife scan measurement of the central illumination lobe width. We used random distribution for the object function. The probe update started after the 25th iteration. Fig. 9(a) shows the reconstructed sample phase. Comparison between this image and an SEM image showed a faithful reproduction, suggesting that the scanning positions were reasonably accurate. We do however note the distortions in the reconstructed characters and letters as well as shadowing. There are also clearly distortions in the retrieved spoke whose average length was 6.16 μm as opposed to the designed value of 5.96 μm.

Using exactly the same starting parameters we re-ran the algorithm for 200 iterations with position refinement, initiating on the 5th iteration with automatic β adjustment as detailed above. The resulting phase image is provided in Fig. 9(b). We note that much of the shadowing and the reconstruction artifacts have now been resolved. In particular the inset shows a significant improvement in the contrast and sharpness of the lithographed lettering; it appears the resolution of the sharp edges is improved as well. The average spoke length was 5.99 μm, matching the design specifications to the nearest pixel. We also note the improved clarity in the "spots" within the spoke reconstruction, e.g., the one indicated by the arrow in Fig. 9(b). The presence of these "spots" imperfections was consistent throughout all our reconstruction tests and is qualitatively similar to the lithographed imperfections seen by SEM. We therefore believe that rather than reconstruction artifacts, they are in fact due to imperfections in the lithographing process. The probe position errors retrieved are shown in Fig. 9(c). The final probe amplitude function is shown in Fig. 9(d). Like with the illumination using Fresnel zone plate (section 4.2), the probe amplitude appeared much cleaner than the reconstruction without using position refinement.

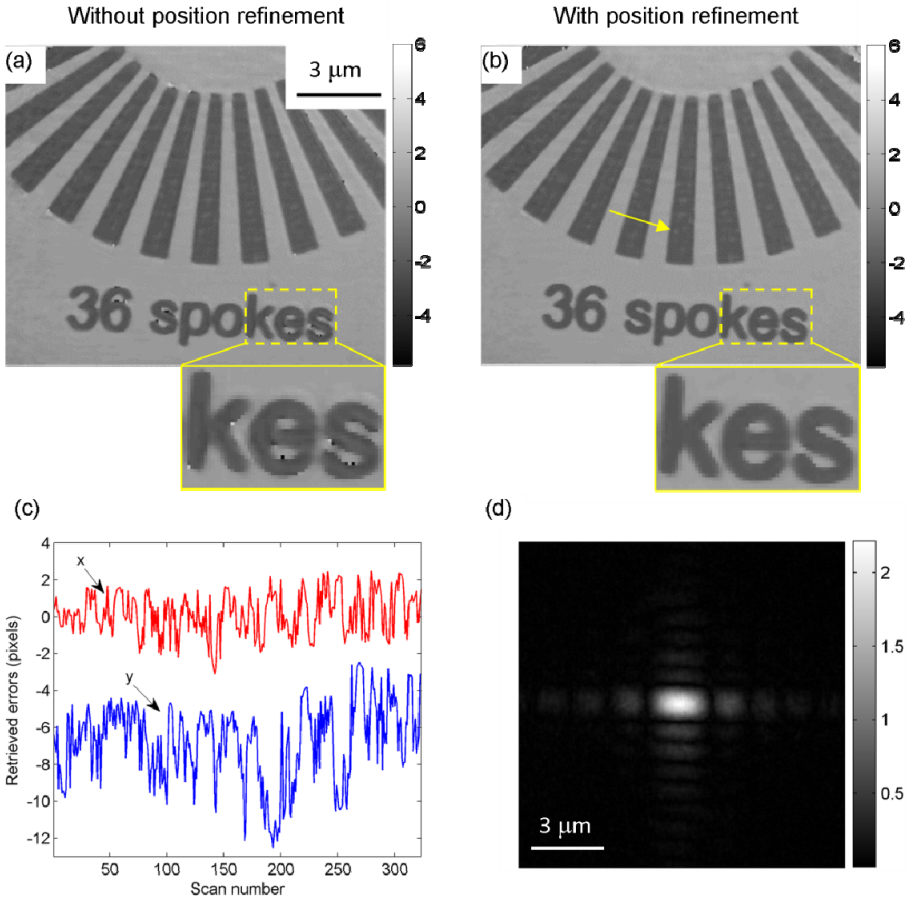

Fig. 9. (a) and (b) Reconstructed object phase without and with position refinement (unwrapped). (c) Retrieved errors at each scan positions, values for y-axis offset by 7 pixels for clarity. (d) Reconstructed probe amplitude with position refinement.

5. Discussion and conclusion

We have proposed and demonstrated a position determination method for ptychography. In the paper, the method was implemented as a natural extension of the ePIE reconstruction

algorithm. The accuracy of the algorithm is determined by how accurately the cross correlation can be performed. This in turn is determined by the actual probe and object functions, the overlap ratio between measurements and the noise level in the data. For objects lacking fine structure, the cross correlation calculation would become less sensitive to the position errors. On the other hand, for such objects, the reconstruction quality will also be more tolerant to position errors. In simulation, our position refinement mechanism has been able to retrieve the sample positions to within a few thousandths' of a pixel accuracy in just several tens of iterations.

The two examples using X-ray data from SLS and APS, using different samples and different kinds of probe, both showed significant improvement of image quality of both object and probe, but with slightly different characteristics. In the SLS case the probe positions arose mainly from a misalignment of the scanning axis directions and the pixel directions of the detector. This is not easy to align in general, but our result indicates that it is important to pay attention to this aspect in the experimental setup. In the APS case, the position errors in Fig. 9(c) had still systematic local variations in which neighbouring scanning positions appear to move together but without the overall rotations found in the first experiment. This might indicate there are linearity issues with the piezo scanners. It is possible that the errors are due to "wobble" motions aggravated by the fact that the encoders of the scan stage are in a different plane from the sample.

In our simulations, early tests suggest that it would be possible to retrieve the translation positions starting from all-zeros guesses using this algorithm and we are investigating this possibility, which could be important for applications such as high resolution metrology. When applying the algorithm to real data, we found that for the algorithm to reliably retrieve the correct positions, the degree of illumination coherence needs to be high. This is understandable since the reconstruction from any coherent component within a partial coherent diffraction data will appear at different scales (temporal partial coherence) or different locations (spatial partial coherence), which would hinder the position error signal finding by cross-correlation. We are currently working on modifying our algorithm to account for partially coherent data to extend its applicability to a broader range of experimental conditions [28].

We believe the proposed method offers a way to exploit the full resolution potential of ptychographic coherent diffractive imaging. The main application of the method would be at short wavelengths where position errors due to system instability and inaccuracy of translation stages would become significant compared to the desired resolution. As shown in our experiments, the method also improves results at longer wavelengths where systematic errors due to misalignment are an issue.

Acknowledgments

The work was supported by the EPSRC basic technology grant under the project Ultimate Microscope (EP/E034055/1) and in part by the EPSRC grant (EP/I022562/1), the Phase Modulation Technology for X-ray Imaging. The X-ray measurements were made at the Swiss Light Source, Paul Scherrer Institute, Villigen, Switzerland, and at APS beamline 34-ID-C, built with US National Science Foundation grant DMR-9724294 and operated by the US Department of Energy, Office of Basic Energy Sciences, under contract no. DE-AC0206CH11357. I.P. is supported by the Australian Research Council Centre of Excellence for Coherent X-ray Science. R.B. acknowledges travel support from the European Community's Seventh Framework Programme (FP7/2007–2013) through grant no. 226716. We would like to thank Mirko Holler for fruitful discussions and Manuel Guizar-Sicairos for critical reading of the manuscript and helpful comments.